Unified structural motifs of the catalytically active state of Co(oxyhydr)oxides during the electrochemical oxygen evolution reaction

Arno Bergmann[1,6]*, Travis E. Jones [2], Elias Martinez Moreno[3], Detre Teschner[2,4], Petko Chernev[3], Manuel Gliech[1], Tobias Reier[1], Holger Dau [3]* and Peter Strasser[1,5]*

Efficient catalysts for the anodic oxygen evolution reaction (OER) are critical for electrochemical H_2 production. Their design requires structural knowledge of their catalytically active sites and state. Here, we track the atomic-scale structural evolution of well-defined $CoO_x(OH)_y$ compounds into their catalytically active state during electrocatalytic operation through operando and surface-sensitive X-ray spectroscopy and surface voltammetry, supported by theoretical calculations. We find clear voltammetric evidence that electrochemically reducible near-surface Co^{3+}–O sites play an organizing role for high OER activity. These sites invariably emerge independent of initial metal valency and coordination under catalytic OER conditions. Combining experiments and theory reveals the unified chemical structure motif as μ_2-OH-bridged $Co^{2+/3+}$ ion clusters formed on all three-dimensional cross-linked and layered $CoO_x(OH)_y$ precursors and present in an oxidized form during the OER, as shown by operando X-ray spectroscopy. Together, the spectroscopic and electrochemical fingerprints offer a unified picture of our molecular understanding of the structure of catalytically active metal oxide OER sites.

The development of stable and earth-abundant inorganic catalysts that split water molecules efficiently is pivotal for developing energy systems based on sustainable and environmentally friendly fuel production and energy storage from renewable power sources[1,2]. Nature utilizes water as the hydrogen source in photosynthesis to convert sunlight into molecular oxygen, electrons and protons. The actual catalytic reaction proceeds in the Mn_4Ca oxo cluster of photosystem II. Its structure and the reaction mechanism were investigated for decades using advanced X-ray-based methods[3–5]. Tremendous efforts have been made to prepare manganese-based inorganic analogues of the active centre of photosystem II[6–9]. However, nickel- and cobalt-based materials exhibit the most promising catalytic activities of the $3d$ metals, with cobalt excelling because of its applicability in neutral and alkaline electrolytes[10–15].

However, extended knowledge of the fundamental activity- and stability-determining properties, and identification of their spectroscopic fingerprints, are essential to tailor improved inorganic water-splitting catalysts. Thus, a deeper understanding of the reaction mechanism, active sites and structural adaption of the catalysts to reaction conditions during the oxygen evolution reaction (OER) is pivotal[16].

Most OER reaction mechanisms are based on O–O bond formation via bulk water nucleophilic attack (BWNA) (Fig. 1c), which proceeds on the terminal oxygen or bridging oxygen (μ-O)[12,17–19]. BWNA has been proposed for photocatalytic OER on Co_3O_4[17]. In contrast, intramolecular oxygen coupling (Fig. 1a, b) is the proposed mechanism for electrocatalytic OER on CoO_x electrocatalysts[20–22],

as supported by density functional theory (DFT) calculations for CoO_x dimers[23], and geminal oxygen coupling (GOC) (Fig. 1a) is the proposed mechanism for cubane-like CoO_x clusters[24]. However, the formation of oxygen ligand holes[24] or, alternatively, a Co(V)–O oxo radical[23], which are prerequisites for GOC, might demand elevated overpotential[19]. Time-resolved Fourier-transform infrared spectroscopy on Co_3O_4 during photocatalytic OER has shown the presence of slow and fast OER sites assigned to electronically isolated and electronically coupled cobalt ions, respectively[19]. Furthermore, the reaction mechanism might depend on the overpotential, as the most active and stable CoO_x surface termination changes with overpotential[18,19].

The participation of μ-O at elevated overpotentials is expected to induce concomitant structural changes of the catalyst. In a previous study, we identified a reversible structural transformation of the near-surface of Co_3O_4 crystallites during moderate oxygen evolution[10]. This transformation was similarly identified in an alkaline electrolyte[25]. The OER can also irreversibly alter the structure of crystalline transition metal phosphates[26] and perovskites[27–29]. In the case of a cobalt phosphate OER electrocatalyst (CoCat)[30], the Co–O bonding environment is contracted during the OER and the di-μ-oxo bridges between cobalt ions show increased disorder compared with the resting state[31]. This finding indicates a change in the protonation pattern of μ-O during the OER. The contraction of the M–O bond can be induced by the oxidation of metal ions[25,31–33] or the generation of electron holes in the oxygen ligand, as was found for IrO_x[34–36]. Furthermore, the metal–oxygen covalency in transition metal perovskites decreases under high-temperature oxygen

[1]The Electrochemical Energy, Catalysis and Materials Science Laboratory, Department of Chemistry, Technical University Berlin, Berlin, Germany. [2]Department of Inorganic Chemistry, Fritz-Haber-Institute of the Max-Planck-Society, Berlin, Germany. [3]Department of Physics, Freie Universität Berlin, Berlin, Germany. [4]Department of Heterogeneous Reactions, Max-Planck-Institute for Chemical Energy Conversion, Mülheim an der Ruhr, Germany. [5]Ertl Center for Electrochemistry and Catalysis, Gwangju Institute of Science and Technology, Gwangju, Republic of Korea. [6]Present address: Department of Interface Science, Fritz-Haber-Institute of the Max-Planck-Society, Berlin, Germany. *e-mail: abergmann@fhi-berlin.mpg.de; holger.dau@fu-berlin.de; pstrasser@tu-berlin.de
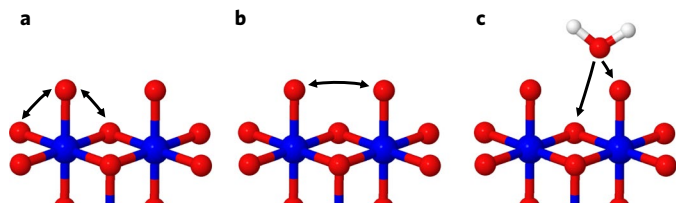
Fig. 1 | Possible mechanisms of O–O bond formation. a, Geminal oxygen coupling (GOC) between a terminal oxygen and a μ-O species. **b**, Intramolecular coupling of two terminal oxygen atoms (IMOC). **c**, Bulk water nucleophilic attack (BWNA).

evolution, showing the redox activity of surface oxygen atoms[37]. The importance of oxygen coordination and redox chemistry was previously pointed out for transition metal perovskites and oxides, as well as for lithium-ion battery electrodes[38–41].

In this work, we prepared four distinct, well-defined Co(oxyhydr)oxide OER model electrocatalysts—a crystalline spinel Co_3O_4, a rock-salt-like CoO (rs-CoO) with purely octahedral Co^{2+} coordination, a wurtzite-like CoO (w-CoO) with tetrahedral Co^{2+} coordination and a layered, heterogenite-like $Co^{2+/3+}O_x(OH)_y$ with low crystallinity denoted as CoOOH (Fig. 2). We investigated their structural and morphological integrity after catalytic operation in a neutral electrolyte using a wide range of bulk and surface-sensitive analytical methods supported by advanced DFT calculations including a Hubbard-like term U (DFT+U) and solution of the Bethe–Salpeter equation (BSE). Our comparative approach enabled us to show that a prevalent structural motif of di-μ-oxo-bridged Co^{3+} ions invariably emerged independent of the initial cobalt coordination and oxidation state, forming an OER-active $CoO_x(OH)_y$ of low(er) crystallinity. We uncovered a contracted bonding environment of oxidized Co–O redox sites during the OER by operando X-ray absorption near-edge structure (XANES) and extended X-ray absorption fine structure (EXAFS) spectroscopy. The emerging unified active site structure concept derived from correlations between the electrochemical Co^{3+}–O reducibility, oxygen coordination and catalytic activity advance our understanding of the OER on Co(oxyhydr)oxides. Our findings could provide generalized structure principles of heterogeneous water splitting beyond cobalt-based electrocatalysts.

Results

Bulk structure of the OER-conditioned $CoO_x(OH)_y$. Identifying structure–activity correlations and investigating the local atomic structure of the catalytically active state demands a kinetically stable state of the electrocatalysts obtained after electrochemical pre-treatment. Therefore, we first investigated the integrity of morphology, crystal and local atomic structure, and cobalt oxidation state of the electrocatalysts after OER conditioning in a neutral, phosphate-containing electrolyte. This OER-conditioned state represents the state of the $CoO_x(OH)_y$ in which the electrochemical and electrocatalytic testing was performed. A detailed description of the as-prepared state is given in Supplementary Section 2. We previously reported that Co_3O_4 did not change its structure irreversibly after OER conditioning[10]. Rietveld refinement of the high-energy X-ray diffraction (HE-XRD) pattern confirmed the strong structural integrity of Co_3O_4 after OER conditioning (Fig. 3, Supplementary Figs. 6–11 and Supplementary Tables 1 and 5).

Similar to Co_3O_4, rs-CoO largely retained its morphology, main structural motifs and crystallinity after OER conditioning (Supplementary Figs. 2–5). However, ellipsoidal crystallites exhibiting surface defects were formed from the spherically shaped ones of the as-prepared state (Fig. 3). The HE-XRD pattern and Rietveld refinement revealed the formation of a spinel-like phase exhibiting a significantly lower coherence length (4.5 ± 0.4 nm) than the as-prepared and residual rs-CoO phase (>9 nm) (Fig. 3, Supplementary
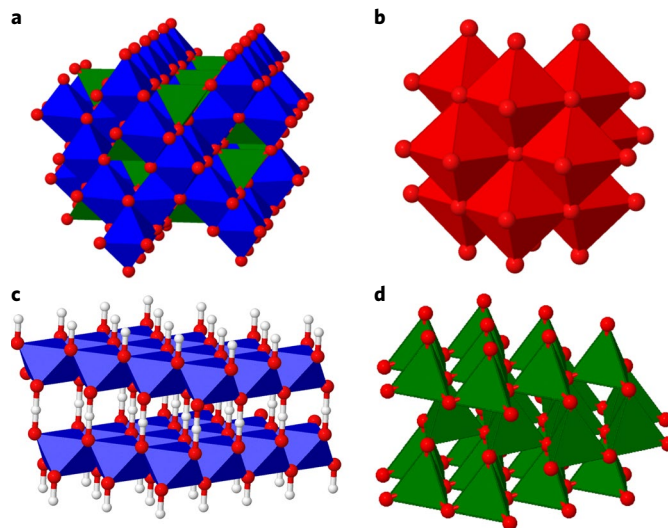

Fig. 2 | Structures of the selected cobalt oxides and cobalt oxyhydroxides. a, Co_3O_4. **b**, rs-CoO. **c**, CoOOH. **d**, w-CoO. The CoO_6 coordination octahedra and CoO_4 coordination tetrahedra are shown. Co^{3+} octahedra, Co^{2+} octahedra and Co^{2+} tetrahedra are shown in blue, red and green, respectively. Hydrogen atoms are shown in white.

Figs. 6 and 7 and Supplementary Table 2). The electrochemically formed spinel phase showed an expanded crystal lattice (with unit cell parameter $a = 8.213 \pm 0.002$ Å) compared with the hydrothermally formed Co_3O_4. We explain this by a higher fraction of Co^{2+} ions on O_h sites in the electrochemically formed spinel, leading to a lower than expected mean oxidation state. Our explanation is supported by a mean cobalt oxidation state that increased slightly after OER conditioning, as determined by the shift of the cobalt K edge (+0.3 eV), which was recorded under operando conditions at +1.2 V (Fig. 4 and Supplementary Table 6). We fitted the k^3-weighted operando EXAFS spectra in a joint-fit approach to avoid over-parameterization and increase the significance of the fit results (further details are provided in the captions of Supplementary Tables 5–8 and Supplementary Figs. 27–29). Our fits revealed that the Co–O and Co–Co distances resembled the Co^{2+} O_h coordination of the as-prepared state (Fig. 5, Supplementary Fig. 10 and Supplementary Table 6). However, a small fraction of shorter Co–O/Co distances appeared (1.905 ± 0.003 and 2.847 ± 0.003 Å), which we assign to di-μ-oxo-bridged Co^{3+} O_h ions within the electrochemically formed spinel phase. Thus, rs-CoO largely resisted strong structural transformation during OER conditioning, but changed partially and irreversibly towards a three-dimensional (3D) cross-linked $Co^{2+/3+}O_x(OH)_y$ of lower crystallinity.

w-CoO exhibited the strongest irreversible structural and morphological change after OER conditioning. The pyramidal shape with hexagonal base of the as-prepared crystallites was retained but the crystal facets were roughened and consisted of significantly smaller domains (Fig. 3 and Supplementary Figs. 2–5). The HE-XRD pattern shows that these smaller domains probably consisted of a spinel-like crystalline phase exhibiting a significantly lower coherence length (3.56 ± 0.11 nm) compared with the as-prepared w-CoO phase (11.8 ± 0.3 nm) (Fig. 3, Supplementary Figs. 6 and 7 and Supplementary Table 3).

The spinel-like lattice was slightly expanded ($a = 8.1173 \pm 0.0013$ Å) compared with the hydrothermally formed Co_3O_4, whereas the w-CoO lattice was contracted compared with the as-prepared lattice (Supplementary Tables 3 and 7). The structural transformation was induced by oxidation of the Co^{2+} T_d ions to Co^{3+} O_h as the cobalt K edge shifted to a higher energy (+0.9 eV) and the mean Co–O length decreased to 1.922 ± 0.005 Å (Figs. 4 and 5, Supplementary
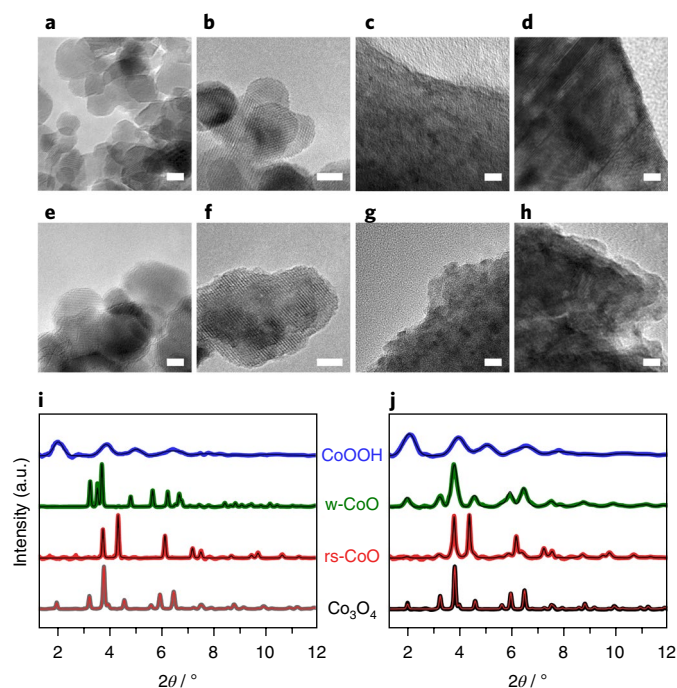
Fig. 3 | Morphological and structural integrity of CoO$_x$(OH)$_y$ electrocatalysts. a–h, Transmission electron microscopy images of Co$_3$O$_4$ (**a** and **e**), rs-CoO (**b** and **f**), CoOOH (**c** and **g**) and w-CoO (**d** and **h**) before (top) and after OER conditioning (bottom). Scale bars: 5 nm. **i, j,** Corresponding HE-XRD patterns of CoO$_x$(OH)$_y$ before (**i**) and after OER conditioning (**j**) were recorded using an incident angle of 1° and 77 keV. Experimental data and fitted profiles from Rietveld refinement are shown by thick and thin lines, respectively. CoO$_x$(OH)$_y$ was refined based on powder diffraction file (PDF) number 00-042-1467 (space group: *Fd*-3*m*) for Co$_3$O$_4$, PDF number 01-078-0431 (space group: *Fm*-3*m*) for rs-CoO, PDF number 01-089-2803 (space group: *P63mc*) for w-CoO and PDF number 01-073-0497 (space group: *R*-3*m*) for CoOOH. The diffraction patterns were background-corrected for clarity. The raw data are shown in Supplementary Fig. 6. The scanning electron micrographs and selected-area electron diffraction patterns are given, respectively, in Supplementary Figs. 2 and 5 for the as-prepared state and Supplementary Figs. 3 and 4 for the OER-conditioned state. Further details on HE-XRD data analysis are given in Supplementary Figs. 6–11 and Supplementary Tables 1–4.

Fig. 10 and Supplementary Table 7). The Co^{3+} ions were octahedrally coordinated and predominantly di-μ-oxo bridged (2.841 ± 0.009 Å), whereas the Co^{2+} T$_d$ ions were primarily mono-μ-oxo bridged to Co^{2+} T$_d$ ions in the residual wurtzite phase (but contracted from 3.217 ± 0.008 to 3.16 ± 0.02 Å; Supplementary Table 7) and Co^{3+} O$_h$ (3.345 ± 0.016 Å) in the spinel-like phase. Thus, w-CoO experienced a significant structural transformation during the OER, leading to 3D cross-linked Co$^{2+/3+}$O$_x$(OH)$_y$ domains of lower crystallinity.

CoOOH consisted of a layered heterogenite-like phase with a structural coherence length smaller than 2 nm before and after OER conditioning, as revealed by HE-XRD (Fig. 3, Supplementary Figs. 6 and 7 and Supplementary Table 4). A strong irreversible oxidation of the initially present Co^{2+} ions to Co^{3+} ions within the CoO$_x$(OH)$_y$ is reflected in the shift of the cobalt K edge (+ 1.7 to 7,720.7 eV) (Fig. 4 and Supplementary Table 8) and the Co–O distance, which changed from two distances (1.898 ± 0.013 and 2.08 ± 0.04 Å for Co^{3+} and Co^{2+}–O, respectively) to a single Co^{3+}–O distance (1.905 ± 0.003 Å). The exclusive Co–Co distance (2.847 ± 0.009 Å) shows that the CoOOH consisted primarily of di-μ-oxo-bridged Co^{3+} O$_h$ ions (Fig. 5, Supplementary Fig. 10 and Supplementary Table 8). Additionally, OER conditioning led to
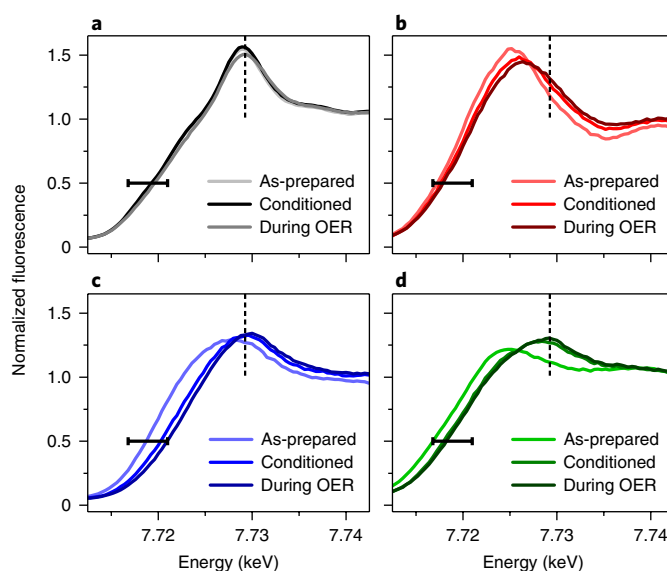

Fig. 4 | Ex situ and operando cobalt oxidation states at selected catalyst states. a–d, Operando XANES spectra collected at the cobalt K edge of Co$_3$O$_4$ (**a**), rs-CoO (**b**), CoOOH (**c**) and w-CoO (**d**) electrocatalysts in the dry state, after OER conditioning at +1.2 V and during the OER in 0.1 M KPi at pH 7. The electrode potential of the catalytically active catalyst state was identified by a current density of 0.5 mA cm^{-2} in an anodic potential scan with a sweep rate of 6 mV s^{-1}. The electrode potential varied between +1.62 and +1.75 V. Co$_3$O$_4$ data were reproduced from previous work and obtained by the freeze-quenched method under potential control[10]. The bar at the half-edge rise denotes the full range of edge positions determined for CoO$_x$(OH)$_y$ and the dashed line represents the white line position of Co$_3$O$_4$ at 7,729 eV. The difference XANES spectra between the OER-conditioned and catalytically active state are shown in Supplementary Fig. 24.

more order in the local atomic structure as the Co–O/Co coordination numbers increased by +1.9 and +3.1, respectively. We note that the Co–O coordination number was less than six, indicating the presence of four- or fivefold coordinated cobalt ions and, thus, empty terminal surface sites. Simultaneously, a more structured surface of the CoO$_x$(OH)$_y$ film appeared and their domains were distinguishable only after OER conditioning (Fig. 3 and Supplementary Figs. 2–5). Thus, we consider the layered CoOOH after OER conditioning as a phosphate-free analogue of CoCat[42].

We conclude that both rs-CoO and w-CoO transformed during OER conditioning irreversibly and independent of the initial cobalt coordination towards a 3D cross-linked Co$^{2+/3+}$O$_x$(OH)$_y$ with primarily di-μ-oxo-bridged Co^{3+} O$_h$ ions of significantly lower crystallinity during the OER. w-CoO transformed stronger than rs-CoO, and CoOOH retained its layered oxyhydroxide structure. Furthermore, the morphological changes (especially the roughening of the w-CoO crystallites) indicate that the structure changed predominantly on the near-surface, calling for detailed near-surface analysis.

Near-surface structure of the OER-conditioned CoO$_x$(OH)$_y$. We then investigated the near-surface (electronic) structure of the as-prepared CoO$_x$(OH)$_y$ and after OER conditioning by total electron yield XANES spectroscopy at the cobalt L$_3$- and O K edges, which probes less than 5 nm deep[43,44]. To assign the resonances of the XANES spectra, we performed DFT + U, BSE and ab initio crystal field multiplet calculations on the as-prepared structures and on layered CoO$_x$(OH)$_y$ structural models exhibiting selected defect motifs (Supplementary Fig. 1). We found very good agreement between experimental and calculated cobalt L$_3$ and O K edge
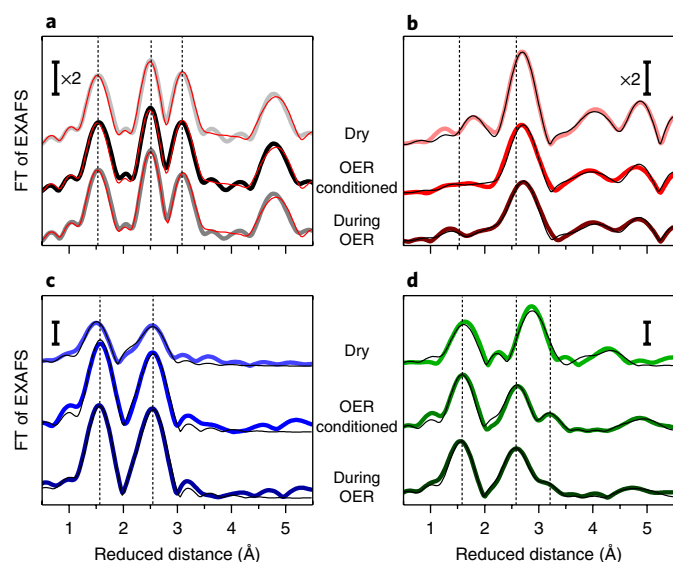
Fig. 5 | Ex situ and operando structural characterization at selected catalyst states. a–d, Fourier transforms (FTs) of operando EXAFS spectra collected at the cobalt K edge of Co_3O_4 (**a**), rs-CoO (**b**), CoOOH (**c**) and w-CoO (**d**) electrocatalysts before (top curves) and after OER conditioning at +1.2 V (middle curves), and during the OER (bottom curves) in 0.1 M KPi at pH 7. The electrode potential of the catalytically active state was identified by a current density of 0.5 mA cm^{-2} in an anodic potential scan with a sweep rate of 6 mV s^{-1}. The electrode potential (not iR-corrected) varied between +1.62 and +1.75 V. Experimental data and fitted profiles are shown by thick and thin lines, respectively. Co_3O_4 data were reproduced from previous work and obtained by the freeze-quenched method under potential control using liquid N_2 after 15 min at 1.62 V in 0.1 M KPi[10]. The dashed vertical lines represent the reduced distance of Co^{3+}–O, di-μ-oxo bridges between pairs of Co^{3+}, and mono-μ-oxo bridges between Co^{2+} T_d and Co^{3+} O_h, at 1.53, 2.51 and 3.08 Å, respectively. Further details on data analysis are provided in the captions of Supplementary Tables 5–8. See also Supplementary Fig. 10 for the k^3-weighted EXAFS spectra, and Supplementary Figs. 25 and 26 for smaller excerpts of the Fourier-transformed EXAFS in the OER-conditioned and catalytically active state. Error plots and confidence intervals of the fits are shown in Supplementary Figs. 27–29.

Fig. 6 | Near-surface oxygen chemistry in $CoO_x(OH)_y$ before and after OER conditioning. a,c, Experimental O K XANES spectra of $CoO_x(OH)_y$ as recorded in total electron yield mode before (**a**) and after OER conditioning (**c**). The contribution of hybridized states between $O_{μ3/4}$ and low-spin Co^{3+} at ~530.5 eV, and between protonated $O_{μ2}$ and high-spin $Co^{2+/3+}$ at ~531.5 eV are shown as shaded areas in magenta and purple, respectively. **b,** Theoretical O K XANES spectra of the ideal, as-prepared cobalt oxides. **d,** Selected oxygen configuration in layered CoOOH. The selected defect motifs are shown in Supplementary Fig. 1. The spectrum of CoOOH in the OER-conditioned state is generated by the calculated spectra of μ$_3$-O and μ$_3$-OH bound to low-spin Co^{3+}, corresponding to the spectrum of the ideal CoOOH structure (magenta) and of μ$_2$-OH bound to high-spin Co^{3+} and high-spin Co^{2+} (purple), as seen by spectral deconvolution of the spectrum of CoOOH after OER conditioning at the bottom of **d**). The calculated mean spectra of the μ$_3$-O/OH bridges in a partially reduced CoOOH structure (that is, bound to high-spin Co^{3+} and Co^{2+} (brown)) mainly contribute to the as-prepared state of CoOOH, as seen in the deconvolution of the CoOOH spectrum at the bottom of **b**. These μ-O bridging motifs were selected to simulate common surface oxygen bridging motifs of Co(oxyhydr)oxides and are shown in Supplementary Fig. 1. Further details of the DFT calculations are given in the Supplementary Methods.

spectra for the as-prepared state (Fig. 6 and Supplementary Fig. 11) and, thus, we confirmed the presence of the cobalt coordination and oxidation state also for the near-surface of the Co(oxyhydr)oxides. The irreversible oxidation of Co^{2+} to Co^{3+} within $CoO_x(OH)_y$ during the OER conditioning determined for the bulk was significantly stronger at the near-surface. The main cobalt L_3 XANES feature of rs-CoO and w-CoO shifted by ~1.7 eV towards CoOOH, which largely resembled the as-prepared state, as was found for Co_3O_4 (Supplementary Fig. 11). Linear combination fitting of the cobalt L_3 XANES spectra revealed only 30% of remnant Co^{2+} ions (Supplementary Fig. 12).

The Co–O bonding at the near-surface of the Co(oxyhydr) oxides after OER conditioning unifies as the cobalt oxidation state. This leads to a similar hybridization between oxygen 2*p* and cobalt 3*d* orbitals, which is probed in the pre-edge of the O K XANES spectra below 534 eV (Fig. 6). The strong variation in the Co–O bonding distance in the as-prepared state is reflected in the pre-edge resonances. By comparison with calculated O K XANES spectra, we were able to assign the energy resonance at ~530.5 eV to low-spin Co^{3+}–O hybridized states in which the oxygen ions are three- or fourfold metal coordinated ($O_{μ3/4}$) in Co_3O_4 and ideal Co^{3+}OOH. The resonance at 533 eV can be assigned to threefold metal-coordinated oxygen or OH bridging pairs of high-spin Co^{2+} and Co^{3+} for
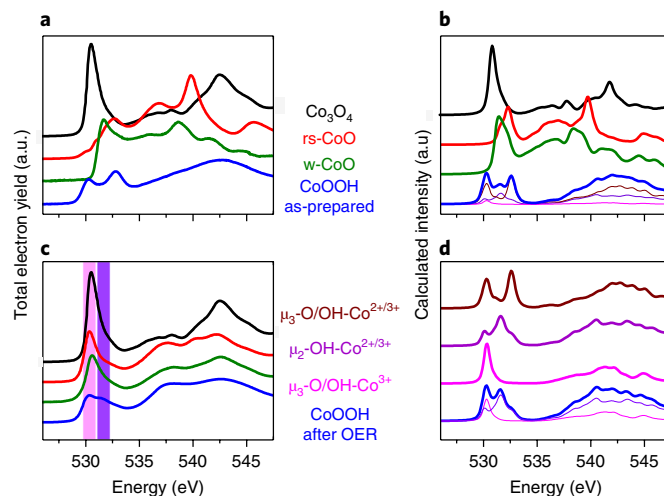
CoOOH, as well as sixfold metal-coordinated oxygen ions bridging pairs of high-spin Co^{2+} for rs-CoO.

After OER conditioning, the pre-edge of the Co(oxyhydr)oxides did not exhibit a prominent Co^{2+}–O resonance (533 eV), but a resonance at ~531.5 eV appeared in addition to the low-spin Co^{3+}–O resonance. The intensity ratio between these two features differs significantly between Co_3O_4 (strong 530.5 eV resonance) and CoOOH (almost equal-intensity contribution). rs-CoO and w-CoO exhibited an intermediate intensity ratio after OER conditioning. To assign the resonance at 531.5 eV, we also performed DFT + U + BSE calculations on defective, layered $CoO_x(OH)_y$ structural models simulating surface-typical bridging oxygen configurations (Supplementary Figs. 1 and 30). We found the best agreement for hybridized states of protonated, twofold metal-coordinated oxygen atoms (μ$_2$-OH) bridging pairs of fivefold oxygen-coordinated high-spin Co^{3+} and Co^{2+} ions. These μ$_2$-OH bridges are predominantly present at edges, corners and metal vacancies in the $CoO_x(OH)_y$ domains, as well as at specific single-crystal terminations; for example, Co_3O_4(110)[45,46]. Thus, we conclude that the area ratio between the two resonances represents the ratio of $O_{μ3}$ and $O_{μ2\text{-}OH}$ sites in $CoO_x(OH)_y$. Additionally, the near-surface composition (as determined by X-ray photoelectron spectroscopy (XPS)) before and after OER conditioning showed that the structural transformation of rs-CoO and w-CoO is accompanied by phosphate incorporation at the near-surface of $CoO_x(OH)_y$ (P/Co ~ 0.4) (Supplementary Figs. 13–17

and Supplementary Table 9). See the Supplementary Methods for details of the theoretical calculations and XPS measurements.

Thus, the electronic structure in the near-surface of the Co(oxyhydr)oxides unified after OER conditioning. However, the differences in the present Co–OH$_x$ units depend on the initial (local atomic) structure and degree of structural transformation during the OER. We consider these differences to be highly important for the electrochemical and electrocatalytic properties.

Local atomic structure of the catalytically active state. We conducted operando cobalt K edge X-ray absorption spectroscopy on the OER-conditioned CoO$_x$(OH)$_y$ under OER conditions, which is a powerful technique to determine the local atomic structure and metal oxidation state in the catalytically active state on inter alia (3d) transition metal oxides[31,47,48] (Figs. 4 and 5). We revealed that the mean cobalt oxidation state of all four CoO$_x$(OH)$_y$ is higher than in the catalytically silent state at 1.2 V. Thus, the electrochemically active cobalt ions are oxidized to +3, +4 or higher during the OER. The fraction of oxidized cobalt ions in CoO$_x$(OH)$_y$ during the OER increased in the order rs-CoO ~ w-CoO < Co$_3$O$_4$ < CoOOH (as determined by the edge shift of 0.1–0.6 eV). CoOOH formally exhibited 22% Co^{4+} ions assuming an edge shift of 2.3 eV per oxidation state and an energy of 7,720.9 eV for Co^{3+} ions[31]. The oxidation of the cobalt ions during the transition to the catalytically active state was accompanied by a larger fraction of Co–O distances that were contracted by ~0.01–0.02 Å in the case of CoO and CoOOH (Fig. 5, Supplementary Fig. 10 and Supplementary Tables 5–8). This contraction can be induced by the formation of electron holes in the oxygen ligand[34–37] or by the oxidation of metal ions[25,31–33]. The cobalt ions in CoOOH are solely sixfold oxygen coordinated during the OER, which is in contrast with the lower Co–O coordination number determined at 1.2 V. The number of di-μ-oxo bridges between Co$^{3+/4+}$ is higher during the OER and, in the case of w-CoO, we identified a lower fraction of mono-μ-oxo bridges between Co^{2+} T$_d$ and Co^{3+} O$_h$ ions similar to Co$_3$O$_4$[10]. The length and order of the di-μ-oxo bridges between pairs of Co$^{3+/4+}$ ions in CoO and CoOOH during the OER decreased only slightly beyond the error of the fit, indicating a slight decrease in the protonation of μ-oxo bridges. Thus, we conclude that the preferred structural motifs under OER conditions are independent of the initial cobalt coordination and oxidation state, and consist of di-μ-oxo-bridged Co$^{3+/4+}$ O$_h$ ions with a contracted CoO$_6$ bonding environment.

Electrochemical characterization. We investigated redox electrochemistry and electrocatalytic properties of the four Co(oxyhydr) oxides after OER conditioning to establish structure–activity correlations of the OER electrocatalysts. We found two redox transitions cathodic to the OER catalytic wave at ~1.4 V (oxidation wave A1, reduction wave C1 in Fig. 7) and at ~1.55 V (A2 and C2) that are commonly attributed to the Co^{2+}/Co^{3+} and Co^{3+}/Co^{4+} redox couples, respectively[31] (Fig. 7a–d). Thus, the local atomic structure at 1.2 V (Figs. 4 and 5) represents the reduced state, which showed a mean oxidation state of around +3 for CoOOH. Therefore, we conclude that the redox couples represent the redox electrochemistry of the surface Co–O sites of CoO$_x$(OH)$_y$ domains rather than bulk oxidation state changes. Of note, the Co^{3+}/Co^{4+} redox potential of layered CoOOH was ~50 mV higher than that of 3D cross-linked CoO$_x$(OH)$_y$.

The surface redox electrochemistry of CoO$_x$(OH)$_y$ strongly depends on its initial structure as the intensity ratio between the two redox transitions varies. Both redox transitions were equally strong for CoOOH, whereas the Co^{3+}/Co^{4+} transition dominated for Co$_3$O$_4$, and rs-CoO and w-CoO exhibited intermediate behaviour. Thus, we conclude that not all Co–O redox sites that undergo the Co^{4+}/Co^{3+} transition have to follow the Co^{3+}/Co^{2+} transition. Therefore, the two redox transitions appear convoluted by (at least)
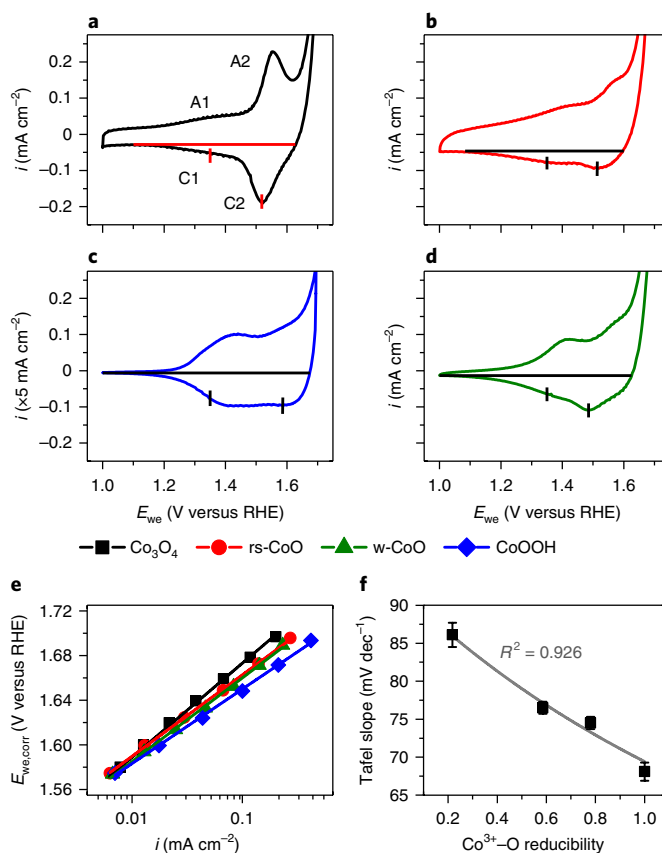

Fig. 7 | Redox electrochemistry and OER catalytic activity of CoO$_x$(OH)$_y$ in a neutral electrolyte. a–d, Cyclic voltammograms of Co$_3$O$_4$ (**a**), rs-CoO (**b**), CoOOH (**c**) and w-CoO (**d**). **e**, Tafel plots of CoO$_x$(OH)$_y$ recorded in de-aerated 0.1 M KPi at pH 7 after OER conditioning. **f**, Tafel slope versus Co^{3+}–O reducibility of CoO$_x$(OH)$_y$ as determined from the cyclic voltammograms and Tafel analysis. All potentials denoted with $E_{we,corr}$ are corrected for Ohmic losses using electrochemical impedance spectroscopy. **a–d** were recorded with 50 mV s^{-1} and show two redox features at ~1.4 V (A1/C1) and ~1.54–1.60 V (A2/C2), respectively. **e** was extracted from anodic potential step rotating disc electrode experiments after equilibration for 4 min at each potential. Each line represents the fit used to extract the Tafel slopes, which are 86, 74, 76 and 68 mV dec^{-1} for Co$_3$O$_4$, rs-CoO, w-CoO and CoOOH, respectively. The error bars in **f** denote the standard error of the fit results. The Co^{3+}–O reducibility was estimated from the capacitance-corrected current ratio C1/C2 normalized to 1 for the ratio of CoOOH. The selected electrode potentials (local minimum for C2 and 1.35 V for C1 to reduce overlap with C2) and base lines used for capacitance correction are denoted in the cyclic voltammograms as horizontal lines. The fit in **f** was performed using $b^* = 2.302 \times RT/(F \times (1 - \gamma \times (1 - K \times C1/C2)))$, yielding $\gamma = 0.361 \pm 0.013$ and a factor $K = 0.60 \pm 0.04$. Therein, b^* denotes the calculated Tafel slope, R the universal gas constant, T the temperature and F the Faraday constant. γ and K represent the interaction and deprotonation factor as defined in Supplementary Section 3. A specific activity at +1.69 V of 0.69, 0.76, 1.13 and 0.63 μA cm$^{-2}_{ECSA}$ for Co$_3$O$_4$, rs-CoO, w-CoO and CoOOH was determined. The electrochemically active surface area (ECSA) was determined using impedance spectroscopy (Supplementary Fig. 21). A comparison with state-of-the-art electrocatalysts in near-neutral and alkaline electrolytes is shown in Supplementary Tables 11 and 12. R^2 denotes the coefficient of determination of the fit.

two structurally different Co–O redox sites. Following the given assignment, we interpret the capacitance-corrected current ratio of the two reduction waves (C1 and C2 as denoted in Fig. 7a–d) as the mean reducibility of the Co^{3+}–O sites. This reducibility increased in

the order of $Co_3O_4 < $ w-CoO $<$ rs-CoO $<$ CoOOH and will become a key descriptor of activity. As for the redox electrochemistry, the electrocatalytic properties of the four Co(oxyhydr)oxides exhibited a gradual transition from Co_3O_4 to CoOOH (Fig. 7e). At the onset of OER (~+1.57 V), the current density (at identical cobalt loading) was similar, but the Tafel slope and, thus, maximal current density differed strongly. The Tafel slope varied between 68 mV dec^{-1} for CoOOH and 86 mV dec^{-1} for Co_3O_4, while rs-CoO and w-CoO exhibited intermediate behaviour. A Tafel slope of 59 mV dec^{-1} is typical for the CoCat[22,49] and seems to be the lowest limit in neutral phosphate buffer. We explain the larger apparent Tafel slopes with a modulation of the overpotential dependence of the OER rate-determining step present during anodic polarization that depends on the near-surface structure of $CoO_x(OH)_y$.

Discussion

We have shown that, during OER conditioning, Co^{2+} oxides transform irreversibly into Co^{3+} O_h-containing $CoO_x(OH)_y$ with lower crystallinity, whereas crystalline Co_3O_4 does not change its structure. The structural transformation occurred largely in the near-surface region, which we probed using electron yield spectroscopy, and invariably evolved into a precursor-independent unified local atomic and electronic structure. We consider the residual Co^{2+} oxides as irrelevant for OER electrocatalysis as the kinetics of their structural transformation was significantly slower. However, no final conclusion regarding the long-term resistance against bulk oxidation[26] can be made based on the present results.

Using operando methods, we identified a structurally unified catalytically active state of $CoO_x(OH)_y$ catalysts exhibiting a higher mean cobalt oxidation state, which qualitatively follows the population of redox active Co–O sites. Additionally, a contracted CoO_6 bonding environment with similar Co–Co cross-linking compared with the resting state at 1.2 V was determined. This contraction was not determined for the near-surface restructuring of Co_3O_4 due to the low fraction of active cobalt ions, but is in accordance with findings in CoCat and CoO_x nanoparticles[31,32]. The contraction of the CoO_6 bonding environment is caused by the oxidation of Co–O redox sites anodic of the Co^{3+}/Co^{4+} redox potential. The change in the cobalt K XANES spectra suggests oxidation of the metal ion to Co^{4+} (ref. [31]). However, the lower charge transfer energy in $Co^{3+/4+}O_x(OH)_y$ also allows the formation of hole density on the oxygen ligand, as identified for $IrO_x(OH)_y$[34–37]. Recently, the formation of a similar species during the OER above the Co^{3+}/Co^{4+} transition was identified for a $CoO_x(OH)_y$ electrocatalyst[50]. Previously, we have identified a reversible, structural transformation of the near-surface of Co_3O_4 crystallites during the OER[10]. In this work, we also observed this kind of restructuring for the catalytically active state of w-CoO because the ratio between mono- and di-μ-oxo bridges declined during the OER.

Following recent DFT calculations on the redox chemistry of Co_3O_4 surfaces[45], we explain this change in site occupancy of the Co^{2+} T_d ions to empty O_h sites with the μ-O vacancy formation in the reaction zone during the OER, as calculated for the $Co_3O_4(100)$ surface. These oxygen vacancies also probably migrate into the subsurface; thus, we consider this process to induce the restructuring of the near-surface at elevated O_2 evolution rates. Oxygen vacancy formation on the $Co_3O_4(110)$ surface has less impact on the local atomic structure[51].

Despite the similarities of the bulk structural motifs after and during the OER, we have observed substantial differences in the surface redox electrochemistry and Tafel behaviours of the four Co(oxyhydr)oxides in neutral phosphate buffer, which correlate strikingly with their near-surface electronic structures. The Tafel slopes decreased as the mean electrochemical reducibility of the Co^{3+}–O sites increased, providing evidence that this reducibility is closely correlated to favourable electrocatalytic properties (Fig. 7f).

We note that better electrocatalytic properties with a more pronounced Co^{2+}/Co^{3+} redox transition were also identified in phosphate-free, alkaline reaction conditions (Supplementary Figs. 22 and 23). In addition, we state that the redox charge of Co^{2+}/Co^{3+} is a better descriptor of the OER active site density than the overall number of redox sites (Supplementary Figs. 20 and 21).

Above all, the electrochemical and electrocatalytic properties are correlated with the near-surface electronic structure and degree of defects in $CoO_x(OH)_y$ (Fig. 8, Supplementary Section 3 and Supplementary Figs. 8 and 9). A higher fraction of the $O_{μ3/4}$ bridging low-spin Co^{3+} ions and lower degree of microstrain in the $CoO_x(OH)_y$ lattice is invariably coupled to a higher fraction of electrochemically irreducible Co^{3+}–O sites and a higher Tafel slope. Vice versa, the highest reducibility and lowest Tafel slope was obtained for the strongest contribution of μ$_2$-OH sites to the O K XANES spectra and the strongest microstrain (Fig. 6d and Supplementary Figs. 8 and 9). Thus, we attribute the reducible Co^{3+}–O sites to μ$_2$-OH bridges between two electronically coupled high-spin cobalt ions that are, thus, highly conducive for fast OER electrocatalysis. This important finding establishes a direct link between the catalytic charge transfer rate and local structure.

We propose that the apparent Tafel slope variations are caused by the chemical environment of the catalytically active site that controls O–O bond formation. While in virtually all proposed mechanisms, terminal oxygen sites are involved in the generation of O–O bonds, leading eventually to molecular oxygen, we hypothesize here that their neighbouring μ$_2$-O ligands are decisive for the catalytic activity as they enable deprotonation of water molecules during BWNA. In highly defective $CoO_x(OH)_y$, the majority of terminal oxygen sites are located adjacent to the μ$_2$-OH sites[52] and the electrochemical reducibility is maximal because both μ$_2$-O and terminal oxygen sites can get protonated in the formal Co^{4+}/Co^{3+} and Co^{3+}/Co^{2+} redox transitions, respectively. Deprotonating μ$_2$-OH increases the disorder of the Co–Co distance, which we and others[31] determined, and the oxidation can lead to differences in the electronic structure[50]. In contrast, (single crystal) oxide surfaces with low defect density, such as the most stable $Co_3O_4(100)$ surface, exhibit primarily terminal oxygen sites adjacent to unprotonated, irreducible μ$_3$-O sites[52]. Thus, these terminal oxygen sites probably cause the single Co^{3+}/Co^{4+} redox transition.

Consequently, we claim that the onset of the catalytic OER is intimately coupled to the formal Co^{3+}/Co^{4+} redox transition leading to protonatable μ$_2$-O sites as well as oxidized $Co^{+3+δ}$ ions bound to terminal $O^{-(2-δ)}$ ligands. The electron hole density $δ$ is possibly shared and itinerant due to the small-to-negative charge transfer energy in $Co^{3+/4+}O_x(OH)_y$[34–37]. Subsequently, the water molecules can be oxidized during BWNA, forming peroxo species with the terminal oxygen for which the μ$_2$-O sites accept the protons and the electrons reduce the neighbouring, electronically coupled $Co^{+3+δ}$–$O^{-(2-δ)}$. In this framework, the absence or limited availability of proton-accepting μ$_2$-O sites can significantly hamper (or even inhibit) deprotonation of water molecules and, thus, OER. Specifically, a low density of μ$_2$-O sites can increase an interaction against rearranging the protons and electrons, leading to a Frumkin-like isotherm of water oxidation. A detailed microkinetic analysis shows that the variation in the Tafel slope, b, with electrochemical reducibility in a neutral electrolyte, can be described by $1/b = 1/b_{min} - γ × \left(1 - K × \frac{C1}{C2}\right)/b_{min}$. Therein, the interaction term $γ$ increases with interaction energy, whereas the (deprotonation) term K increases with the equilibrium constants of Co^{3+}–O oxidation and μ$_2$-OH deprotonation. A similar formalism can be derived for the case of O–O bond formation between the terminal oxygen and μ$_2$-O. We did not identify a correlation between phosphate adsorption and electrocatalysis, which is in line with previous findings that only phosphate depletion hampers oxygen evolution[22]. However, low solubility of Co^{2+} in a neutral phosphate buffer can prevent significant loss of Co^{2+} ions

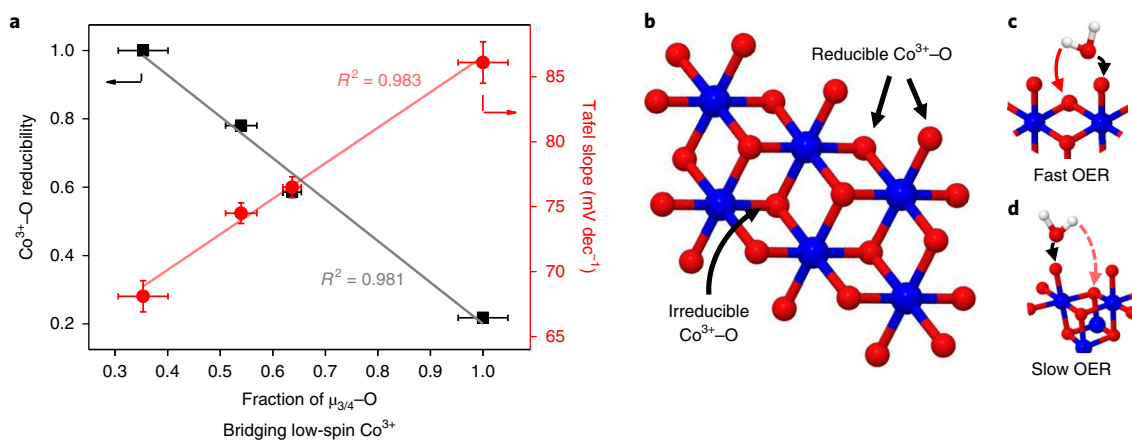**Fig. 8 | Correlation of near-surface chemistry with electrochemical reducibility and catalytic activity. a**, Correlation of the mean Co^{3+}–O reducibility and Tafel slope with the normalized fraction of $\mu_{3/4}$ bridging low spin Co^{3+} ions. **b**, Structural model of a layered CoO$_x$(OH)$_y$. **c**, Schematic of fast, unified OER sites. **d**, Schematic of slow and irreducible OER sites. The proposed catalytic functions towards O–O bond formation and H$_2$O deprotonation are indicated by black and red arrows, respectively. The mean Co^{3+}–O reducibility and Tafel slopes were determined from cyclic voltammetry (Fig. 7a–d) and quasi-stationary potential step experiments, respectively, in de-aerated 0.1 M KPi at pH 7. The Co^{3+}–O reducibility was estimated from the capacitance-corrected current ratio C1/C2 normalized to 1 for CoOOH. The selected electrode potentials (local minimum for C2 and 1.35 V for C1 to reduce overlap with C2) and base lines used for capacitance correction are denoted in the cyclic voltammograms (Fig. 7a–d). The Tafel slope was extracted from a fit of the E–log[i] profile determined by the quasi-stationary potential step experiments (Fig. 7e). The fraction of low-spin Co^{3+}–O sites was determined from peak fitting of the pre-edge feature of the O K XANES spectra, determining the degree of hybridization between 3d orbitals of low-spin Co^{3+} and 2p orbitals of neighbouring oxygen, using the 530 eV resonance. The orbital hybridization was normalized to the area of the 530 eV resonance of Co$_3$O$_4$ (Fig. 6 and Supplementary Fig. 17). The error bars represent the standard errors of the corresponding fits. R^2 denotes the coefficient of determination of the linear regression.

during the OER due to phosphate complexation (precipitation) and its re-oxidation on the catalyst surface. In alkaline electrolyte, the presence of OH$^-$ enhances O–O bond formation via nucleophilic attack, and the deprotonation of the reaction intermediates leads to significantly smaller variation of the Tafel slope. The formation of proton-deficient surface oxygen sites is thought to play an important role for NiOOH electrocatalysts in alkaline electrolytes[53] (see Supplementary Discussion for further details).

Interestingly, the largest Tafel slope was determined for the crystalline Co$_3$O$_4$ and is accompanied by an overpotential-dependent restructuring (for example, Co^{2+} T$_d$ to Co$^{3+/4+}$ O$_h$)[20,21]. The restructuring under elevated OER conditions forms a dynamic reaction zone of kinetically limited thickness[54], which exhibits strong structural similarities to delithiated cubic LiCoO$_2$[55]. The electronic structure of this Li$_{1-x}$CoO$_2$ is characterized by delocalized t$_{2g}$ holes, which we think decreases the interaction term γ, and the restructuring probably forms additional μ_2-O (deprotonation) sites. Consequently, the rate-determining step, dominant OER catalytic processes and cathodic Tafel slope converge in a neutral electrolyte (Supplementary Figs. 18 and 19). Thus, besides the difficulty in ambiguously specifying the sequence of reactions steps during the OER based on electrokinetic analysis, we conclude from our findings that the reducible Co^{3+}–O sites that are present in layered and 3D cross-linked CoO$_x$(OH)$_y$ are ultimately decisive for high OER activity.

Furthermore, we note that our results are in very good conceptual agreement with recent findings for CoO$_x$ photocatalysis where two Co–O sites exhibit distinct differences in OER kinetics and Co–O bonding environment[17]. Previously, correlations between the cobalt oxide redox transitions, OER activity and domain size were formulated in the case of alkaline electrolytes[14,32,39]. We also note the conceptual similarity to iridium-based electrocatalysts that exhibit distinct redox behaviour, specific activity and Tafel slopes depending on the domain size and presence of hydroxylated oxygen species[56–58]. Similar to CoO$_x$(OH)$_y$, a near-surface (electronic) structure containing O$^-$ sites in a defective IrO$_x$(OH)$_y$ is accompanied by higher catalytic activity, and the fraction of these sites increases with current density[36,59,60].

In summary, we have identified a fundamental and highly important structure–activity correlation for OER electrocatalysts, as exemplified by Co(oxyhydr)oxides. We have shown that cobalt-based electrocatalysts transform—independent of their initial cobalt coordination and oxidation state—into universal structural motifs under electrocatalytic conditions. In contrast with Co$_3$O$_4$, the crystal structure of Co^{2+} oxides exhibited limited integrity at the near-surface, as they transformed towards 3D cross-linked CoO$_x$(OH)$_y$ with predominantly octahedrally coordinated, di-μ-oxo-bridged Co^{3+} ions. Above all, we have identified the spectroscopic fingerprints (in the X-ray absorption spectra and cyclic voltammograms) of highly important, electrochemically reducible Co^{3+}–O sites that act as fast OER sites, along with their chemical structure with μ_2-O(H) coordination using DFT + U + BSE calculations. All the results are in very good agreement with earlier experimental findings on OER electrocatalysts and we expect them to evolve into a quite unified mechanistic and active site concept of OER electrocatalysis. We expect our active site concept to aid future research in the development of further advanced water electrolysis electrocatalysts for sustainable hydrogen production and electrochemical energy storage devices.

Methods

Syntheses. All catalysts were prepared on cleaned glassy carbon (HTW) plates with a cobalt loading of 322 nmol cm^{-1}. Films of Co$_3$O$_4$ and rs-CoO were prepared using spin-coating, as described previously[10]. A single layer was deposited at 2,000 r.p.m. Co$_3$O$_4$ films were formed at 400 °C in air for 15 min, whereas rs-CoO was formed in a two-step process. The precursor film was first decomposed at 300 °C in air; afterwards, the CoO was formed at 400 °C for 15 min in 4 vol% H$_2$/Ar. w-CoO was prepared using colloidal, microwave-assisted synthesis based on a published route and subsequent drop-coating[61]. After drop-coating of 322 nmol cobalt cm^{-2}, the samples were heat treated at 60 °C in air and 225 °C in argon for 15 min to remove oleylamine residues. Thin films of CoOOH were prepared using electrodeposition based on a published routine[33]. After deposition, the electrodes were extensively washed using Milli-Q water and dried under nitrogen flow. Further details are given in the Supplementary Information.

Physicochemical characterization. Transmission electron microscope images were recorded at 200 kV using an FEI Tecnai G^2 20 S-TWIN instrument. Samples were scratched off the substrate using a scalpel and transferred onto a lacy carbon-coated copper grid. HE-XRD patterns were recorded at beamline ID 31 at the

European Synchrotron Radiation Facility (ESRF) in Grenoble, operating at 77 keV using a large-area Pilatus 2M CdTe detector. The working distance was calibrated using a CeO$_2$ standard (National Institute of Standards and Technology Standard Reference Material 674b). Rietveld refinement was performed using the Topas software package. XPS and absorption spectra at the cobalt L- and O K edges were collected at the Innovative Station for In Situ Spectroscopy beamline of BESSY II (Berliner Elektronenspeicherring-Gesellschaft für Synchrotronstrahlung m. b. H.) in Berlin[62]. The XANES spectra were recorded under ultra-high vacuum conditions in the total electron yield mode detected with a Faraday cup. The total electron yield (TEY) signals recorded at the cobalt L- and O K edges were normalized using incident and post-edge intensity.

Operando X-ray absorption spectroscopy at the cobalt K edge. Operando X-ray absorption spectroscopy experiments were carried out at the I811 beamline of Max-Lab, Lund. An electrochemical cell for X-ray studies based on the thin-layer concept was used[10]. The electrolyte was constantly degassed with 0.1 M phosphate buffer at pH 7. Ag/AgCl (World Precision Instruments) and a platinum wire acted as reference and counter electrodes, respectively. The working electrode was immersed in the electrolyte at +1.62 V after ex situ characterization and OER-conditioned for 15 min. The OER potential was determined by a current density of 0.5 mA cm^{-2} during the anodic potential scan with 6 mV s^{-1} and maintained for 10 min to ensure stationary conditions. All spectra were recorded in fluorescence mode at an incident X-ray angle of ~2° using a 50 mm^2 Vortex silicon-drift detector. The fluorescence signal was normalized using incident and post-edge intensity. The X-ray energy was calibrated by aligning the first inflection point of the cobalt K edge absorption spectra to 7,709 eV[63]. The freeze-quench measurements of Co$_3$O$_4$ at the cobalt K edge for quasi-in situ experiments were conducted at the KMC-1 bending-magnet beamline of BESSY II at 20 K in a cryostat (Oxford Danfysik) with a liquid-helium flow system. The samples were freeze-quenched under potential control after 15 min at the desired electrode potential using liquid N$_2$ and stored therein until the XAS measurements were performed[10]. k-space fitting of the k^3-weighted EXAFS spectra between 3.0 and 12 or 13 Å^{-1} was performed using an amplitude-reduction factor S_0^2 of 0.75. The coordination numbers (N) were fitted independently, but the distances (R) and Debye–Waller factors (σ) were in parts jointly fitted. Fitting was performed using the software package SimX after calculation of the phase functions using the FEFF programme[64,65]. The error of distance determination represents the relative precision within this study; the absolute distance accuracy of EXAFS is not better than ±0.02 Å. Further details are given in the captions of Supplementary Tables 5–8.

DFT calculations. DFT calculations were performed with the Quantum ESPRESSO[66] package using norm-conserving pseudopotentials. The Perdew, Burke and Ernzerhof exchange and correlation potential was employed along with a Hubbard U on cobalt to account for the on-site Coulomb interaction adopted from Selloni[51,67]. Cobalt oxidation states were assigned using the on-site d occupation matrix[68]. O K edge spectra were computed by a resolvent-based BSE approach using the OCEAN package[69,70]. Further details are given in the Supplementary Methods.

Electrochemical measurements. Electrochemical rotating disk electrode measurements were conducted using a home-made glass cell in a three-electrode configuration with a Pine rotator and a Bio-Logic SP-200 potentiostat. The reference electrodes were a Hg/HgSO$_4$ electrode (Princeton) in a neutral electrolyte and a saturated calomel electrode (Princeton) in an alkaline electrolyte; these were freshly calibrated using a Pt/H$_2$ electrode. The reference electrode was connected to the working electrode compartment via a Haber–Luggin capillary. The counter electrode in both electrolytes was a platinum gauze. Electrochemical experiments were conducted in N$_2$-degassed 0.1 M phosphate buffer (KPi, pH 7) prepared from 0.1 M K$_2$HPO$_4$ and KH$_2$PO$_4$ (>99.99%; Suprapur; Merck) and freshly prepared N$_2$-degassed 0.1 M KOH (99.99%; Sigma–Aldrich). The rotation rate was 400 r.p.m. Cyclic voltammograms were recorded without rotation. For Tafel slope analysis, current density was recorded for potential steps of 20 mV under quasi-stationary conditions, after 4 min of equilibration at each step. All electrode potentials were referred to the reversible hydrogen electrode (RHE) and where denoted were corrected for Ohmic losses determined by electrochemical impedance spectroscopy.

Data availability
The data that support the plots within this paper and other findings of this study are available from the corresponding author upon reasonable request.

References
1. Gray, H. B. Powering the planet with solar fuel. *Nat. Chem.* **1**, 7 (2009).
2. Lewis, N. S. & Nocera, D. G. Powering the planet: chemical challenges in solar energy utilization. *Proc. Natl Acad. Sci. USA* **103**, 15729–15735 (2006).
3. Kupitz, C. et al. Serial time-resolved crystallography of photosystem II using a femtosecond X-ray laser. *Nature* **513**, 261–265 (2014).
4. Dau, H., Zaharieva, I. & Haumann, M. Recent developments in research on water oxidation by photosystem II. *Curr. Opin. Chem. Biol.* **16**, 3–10 (2012).
5. Haumann, M. et al. Structural and oxidation state changes of the photosystem II manganese complex in four transitions of the water oxidation cycle ($S_0 \rightarrow S_1$, $S_1 \rightarrow S_2$, $S_2 \rightarrow S_3$, and $S_{3,4} \rightarrow S_0$) characterized by X-ray absorption spectroscopy at 20 K and room temperature. *Biochemistry* **44**, 1894–1908 (2005).
6. Zaharieva, I. et al. Water oxidation catalysis—role of redox and structural dynamics in biological photosynthesis and inorganic manganese oxides. *Energy Environ. Sci.* **9**, 2433–2443 (2016).
7. Bergmann, A., Zaharieva, I., Dau, H. & Strasser, P. Electrochemical water splitting by layered and 3D cross-linked manganese oxides: correlating structural motifs and catalytic activity. *Energy Environ. Sci.* **6**, 2745–2755 (2013).
8. Hocking, R. K. et al. Water-oxidation catalysis by manganese in a geochemical-like cycle. *Nat. Chem.* **3**, 461–466 (2011).
9. Jiao, F. & Frei, H. Nanostructured manganese oxide clusters supported on mesoporous silica as efficient oxygen-evolving catalysts. *Chem. Commun.* **46**, 2920–2922 (2010).
10. Bergmann, A. et al. Reversible amorphization and the catalytically active state of crystalline Co$_3$O$_4$ during oxygen evolution. *Nat. Commun.* **6**, 8625 (2015).
11. Dionigi, F. & Strasser, P. NiFe-based (oxy)hydroxide catalysts for oxygen evolution reaction in non-acidic electrolytes. *Adv. Energy Mater.* **6**, 1600621 (2016).
12. Hong, W. T. et al. Toward the rational design of non-precious transition metal oxides for oxygen electrocatalysis. *Energy Environ. Sci.* **8**, 1404–1427 (2015).
13. Dincâ, M., Surendranath, Y. & Nocera, D. G. Nickel–borate oxygen-evolving catalyst that functions under benign conditions. *Proc. Natl Acad. Sci. USA* **107**, 10337–10341 (2010).
14. Burke, M. S., Kast, M. G., Trotochaud, L., Smith, A. M. & Boettcher, S. W. Cobalt–iron (oxy)hydroxide oxygen evolution electrocatalysts: the role of structure and composition on activity, stability, and mechanism. *J. Am. Chem. Soc.* **137**, 3638–3648 (2015).
15. Trotochaud, L., Ranney, J. K., Williams, K. N. & Boettcher, S. W. Solution-cast metal oxide thin film electrocatalysts for oxygen evolution. *J. Am. Chem. Soc.* **134**, 17253–17261 (2012).
16. Reier, T., Nong, H. N., Teschner, D., Schlögl, R. & Strasser, P. Electrocatalytic oxygen evolution reaction in acidic environments—reaction mechanisms and catalysts. *Adv. Energy Mater.* **7**, 1601275 (2016).
17. Zhang, M., de Respinis, M. & Frei, H. Time-resolved observations of water oxidation intermediates on a cobalt oxide nanoparticle catalyst. *Nat. Chem.* **6**, 362–367 (2014).
18. Bajdich, M., Garcia-Mota, M., Vojvodic, A., Norskov, J. K. & Bell, A. T. Theoretical investigation of the activity of cobalt oxides for the electrochemical oxidation of water. *J. Am. Chem. Soc.* **135**, 13521–13530 (2013).
19. Plaisance, C. P. & van Santen, R. A. Structure sensitivity of the oxygen evolution reaction catalyzed by cobalt(II,III) oxide. *J. Am. Chem. Soc.* **137**, 14660–14672 (2015).
20. Koroidov, S., Anderlund, M. F., Styring, S., Thapper, A. & Messinger, J. First turnover analysis of water-oxidation catalyzed by Co-oxide nanoparticles. *Energy Environ. Sci.* **8**, 2492–2503 (2015).
21. Ullman, A. M., Brodsky, C. N., Li, N., Zheng, S.-L. & Nocera, D. G. Probing edge site reactivity of oxidic cobalt water oxidation catalysts. *J. Am. Chem. Soc.* **138**, 4229–4236 (2016).
22. Surendranath, Y., Kanan, M. W. & Nocera, D. G. Mechanistic studies of the oxygen evolution reaction by a cobalt-phosphate catalyst at neutral pH. *J. Am. Chem. Soc.* **132**, 16501–16509 (2010).
23. Fernando, A. & Aikens, C. M. Reaction pathways for water oxidation to molecular oxygen mediated by model cobalt oxide dimer and cubane catalysts. *J. Phys. Chem. C* **119**, 11072–11085 (2015).
24. Mattioli, G., Giannozzi, P., Amore Bonapasta, A. & Guidoni, L. Reaction pathways for oxygen evolution promoted by cobalt catalyst. *J. Am. Chem. Soc.* **135**, 15353–15363 (2013).
25. Tung, C.-W. et al. Reversible adapting layer produces robust single-crystal electrocatalyst for oxygen evolution. *Nat. Commun.* **6**, 8106 (2015).
26. González-Flores, D. et al. Heterogeneous water oxidation: surface activity versus amorphization activation in cobalt phosphate catalysts. *Angew. Chem.* **127**, 2502–2506 (2015).
27. Grimaud, A. et al. Double perovskites as a family of highly active catalysts for oxygen evolution in alkaline solution. *Nat. Commun.* **4**, 2439 (2013).
28. Risch, M. et al. Structural changes of cobalt-based perovskites upon water oxidation investigated by EXAFS. *J. Phys. Chem. C* **117**, 8628–8635 (2013).
29. May, K. J. et al. Influence of oxygen evolution during water oxidation on the surface of perovskite oxide catalysts. *J. Phys. Chem. Lett.* **3**, 3264–3270 (2012).
30. Kanan, M. W. & Nocera, D. G. In situ formation of an oxygen-evolving catalyst in neutral water containing phosphate and Co^{2+}. *Science* **321**, 1072–1075 (2008).

31. Risch, M. et al. Water oxidation by amorphous cobalt-based oxides: in situ tracking of redox transitions and mode of catalysis. *Energy Environ. Sci.* **8**, 661–674 (2015).

32. Seo, B. et al. Size-dependent activity trends combined with in situ X-ray absorption spectroscopy reveal insights into cobalt oxide/carbon nanotube-catalyzed bifunctional oxygen electrocatalysis. *ACS Catal.* **6**, 4347–4355 (2016).

33. Friebel, D. et al. On the chemical state of Co oxide electrocatalysts during alkaline water splitting. *Phys. Chem. Chem. Phys.* **15**, 17460–17467 (2013).

34. Mizokawa, T. et al. Role of oxygen holes in Li_xCoO_2 revealed by soft X-ray spectroscopy. *Phys. Rev. Lett.* **111**, 056404 (2013).

35. Van Elp, J. et al. Electronic structure of CoO, Li-doped CoO, and $LiCoO_2$. *Phys. Rev. B* **44**, 6090–6103 (1991).

36. Pfeifer, V. et al. In situ observation of reactive oxygen species forming on oxygen-evolving iridium surfaces. *Chem. Sci.* **8**, 2143–2149 (2017).

37. Mueller, D. N., Machala, M. L., Bluhm, H. & Chueh, W. C. Redox activity of surface oxygen anions in oxygen-deficient perovskite oxides during electrochemical reactions. *Nat. Commun.* **6**, 6097 (2015).

38. Hong, W. T. et al. Tuning the spin state in $LaCoO_3$ thin films for enhanced high-temperature oxygen electrocatalysis. *J. Phys. Chem. Lett.* **4**, 2493–2499 (2013).

39. Han, B. et al. Role of $LiCoO_2$ surface terminations in oxygen reduction and evolution kinetics. *J. Phys. Chem. Lett.* **6**, 1357–1362 (2015).

40. Sathiya, M. et al. Reversible anionic redox chemistry in high-capacity layered-oxide electrodes. *Nat. Mater.* **12**, 827–835 (2013).

41. Luo, K. et al. Charge-compensation in 3d-transition-metal-oxide intercalation cathodes through the generation of localized electron holes on oxygen. *Nat. Chem.* **8**, 684–691 (2016).

42. Du, P, Kokhan, O., Chapman, K. W., Chupas, P. J. & Tiede, D. M. Elucidating the domain structure of the cobalt oxide water splitting catalyst by X-ray pair distribution function analysis. *J. Am. Chem. Soc.* **134**, 11096–11099 (2012).

43. Abbate, M. et al. Probing depth of soft X-ray absorption spectroscopy measured in total-electron-yield mode. *Surf. Interface Anal.* **18**, 65–69 (1992).

44. Ruosi, A. et al. Electron sampling depth and saturation effects in perovskite films investigated by soft x-ray absorption spectroscopy. *Phys. Rev. B* **90**, 125120 (2014).

45. Zasada, F., Piskorz, W. & Sojka, Z. Cobalt spinel at various redox conditions: DFT + U investigations into the structure and surface thermodynamics of the (100) facet. *J. Phys. Chem. C* **119**, 19180–19191 (2015).

46. Zasada, F. et al. Periodic DFT and HR-STEM studies of surface structure and morphology of cobalt spinel nanocrystals. Retrieving 3D shapes from 2D images. *J. Phys. Chem. C* **115**, 6423–6432 (2011).

47. Hu, Y., Bae, I. T., Mo, Y., Scherson, D. A. & Antonio, M. R. In situ X-ray absorption fine structure and optical reflectance studies of electrodeposited nickel hydrous oxide films in alkaline electrolytes. *Can. J. Chem.* **75**, 1721–1729 (1997).

48. Kanan, M. W. et al. Structure and valency of a cobalt-phosphate water oxidation catalyst determined by in situ X-ray spectroscopy. *J. Am. Chem. Soc.* **132**, 13692–13701 (2010).

49. Gerken, J. B. et al. Electrochemical water oxidation with cobalt-based electrocatalysts from pH 0–14: the thermodynamic basis for catalyst structure, stability, and activity. *J. Am. Chem. Soc.* **133**, 14431–14442 (2011).

50. Favaro, M. et al. Understanding the oxygen evolution reaction mechanism on CoO_x using operando ambient-pressure X-ray photoelectron spectroscopy. *J. Am. Chem. Soc.* **139**, 8960–8970 (2017).

51. Selcuk, S. & Selloni, A. DFT plus U study of the surface structure and stability of Co_3O_4(110): dependence on U. *J. Phys. Chem. C* **119**, 9973–9979 (2015).

52. Mattioli, G., Risch, M., Bonapasta, A. A., Dau, H. & Guidoni, L. Protonation states in a cobalt-oxide catalyst for water oxidation: fine comparison of ab initio molecular dynamics and X-ray absorption spectroscopy results. *Phys. Chem. Chem. Phys.* **13**, 15437–15441 (2011).

53. Diaz-Morales, O., Ferrus-Suspedra, D. & Koper, M. T. M. The importance of nickel oxyhydroxide deprotonation on its activity towards electrochemical water oxidation. *Chem. Sci.* **7**, 2639–2645 (2016).

54. Han, B. H. et al. Nanoscale structural oscillations in perovskite oxides induced by oxygen evolution. *Nat. Mater.* **16**, 121–126 (2017).

55. Liu, H. et al. Correlations among structure, electronic properties, and photochemical water oxidation: a case study on lithium cobalt oxides. *ACS Catal.* **5**, 3791–3800 (2015).

56. Bernicke, M. et al. Iridium oxide coatings with templated porosity as highly active oxygen evolution catalysts: structure–activity relationships. *ChemSusChem* **8**, 1908–1915 (2015).

57. Reier, T. et al. Electrocatalytic oxygen evolution on iridium oxide: uncovering catalyst–substrate interactions and active iridium oxide species. *J. Electrochem. Soc.* **161**, F876–F882 (2014).

58. Reier, T. et al. Molecular insight in structure and activity of highly efficient, low-Ir Ir–Ni oxide catalysts for electrochemical water splitting (OER). *J. Am. Chem. Soc.* **137**, 13031–13040 (2015).

59. Pfeifer, V. et al. The electronic structure of iridium oxide electrodes active in water splitting. *Phys. Chem. Chem. Phys.* **18**, 2292–2296 (2016).

60. Pfeifer, V. et al. Reactive oxygen species in iridium-based OER catalysts. *Chem. Sci.* **7**, 6791–6795 (2016).

61. Seo, W. S. et al. Phase- and size-controlled synthesis of hexagonal and cubic CoO nanocrystals. *J. Am. Chem. Soc.* **127**, 6188–6189 (2005).

62. Knop-Gericke, A. et al. in *Advances in Catalysis* Vol. 52 (eds Gates, B. C. & Knözinger, H.) 213–272 (Academic Press, Burlington, 2009).

63. Bearden, J. A. & Burr, A. F. Reevaluation of X-ray atomic energy levels. *Rev. Mod. Phys.* **39**, 125–142 (1967).

64. Ankudinov, A. L., Ravel, B., Rehr, J. J. & Conradson, S. D. Real-space multiple-scattering calculation and interpretation of X-ray-absorption near-edge structure. *Phys. Rev. B* **58**, 7565–7576 (1998).

65. Rehr, J. J. & Albers, R. C. Theoretical approaches to X-ray absorption fine structure. *Rev. Mod. Phys.* **72**, 621–654 (2000).

66. Giannozzi, P. et al. QUANTUM ESPRESSO: a modular and open-source software project for quantum simulations of materials. *J. Phys. Condens. Matter* **21**, 395502 (2009).

67. Chen, J. & Selloni, A. First principles study of cobalt (hydr)oxides under electrochemical conditions. *J. Phys. Chem. C* **117**, 20002–20006 (2013).

68. Sit, P. H. L., Car, R., Cohen, M. H. & Selloni, A. Simple, unambiguous theoretical approach to oxidation state determination via first-principles calculations. *Inorg. Chem.* **50**, 10259–10267 (2011).

69. Vinson, J. & Rehr, J. J. Ab initio Bethe–Salpeter calculations of the X-ray absorption spectra of transition metals at the *L*-shell edges. *Phys. Rev. B* **86**, 195135 (2012).

70. Vinson, J., Rehr, J. J., Kas, J. J. & Shirley, E. L. Bethe–Salpeter equation calculations of core excitation spectra. *Phys. Rev. B* **83**, 115106 (2011).

Author contributions

A.B. prepared all the samples, performed the electrochemical characterization, hard X-ray absorption spectroscopy at Max-Lab and HE-XRD experiments at ESRF, and analysed the data. E.M.M. and P.C. performed the hard X-ray absorption spectroscopy experiments at BESSY II and analysed the corresponding data, D.T. and A.B. performed the XPS and soft X-ray absorption spectroscopy experiments and analysed the data. T.E.J. performed the DFT calculations and wrote parts of the manuscript. M.G. performed the transmission electron microscopy. T.R. performed the scanning electron microscopy and assisted in the X-ray absorption spectroscopy at Max-Lab. A.B., H.D. and P.S. designed the research and experiments and wrote parts of the manuscript.

Competing interests

The authors declare no competing interests.

Additional information

Supplementary information is available for this paper at https://doi.org/10.1038/s41929-018-0141-2.

Reprints and permissions information is available at www.nature.com/reprints.

Correspondence and requests for materials should be addressed to A.B. or H.D. or P.S.

Publisher's note: Springer Nature remains neutral with regard to jurisdictional claims in published maps and institutional affiliations.